# Cold-Starting All-Solid-State Batteries from Room Temperature by Thermally Modulated Current Collector in Sub-Minute

*Yusheng Ye, Wenxiao Huang, Rong Xu, Xin Xiao, Wenbo Zhang, Hao Chen, Jiayu Wan, Fang Liu, Hiang Kwee Lee, Jinwei Xu, Zewen Zhang, Yucan Peng, Hansen Wang, Xin Gao, Yecun Wu, Guangmin Zhou, and Yi Cui\**

All-solid-state batteries (ASSBs) show great potential as high-energy and high-power energy-storage devices but their attainable energy/power density at room temperature is severely reduced because of the sluggish kinetics of lithium-ion transport. Here a thermally modulated current collector (TMCC) is reported, which can rapidly cold-start ASSBs from room temperature to operating temperatures (70–90 °C) in less than 1 min, and simultaneously enhance the transient peak power density by 15-fold compared to one without heating. This TMCC is prepared by integrating a uniform, ultrathin (≈200 nm) nickel layer as a thermal modulator within an ultralight polymer-based current collector. By isolating the thermal modulator from the ion/electron pathway of ASSBs, it can provide fast, stable heat control yet does not interfere with regular battery operation. Moreover, this ultrathin (13.2 μm) TMCC effectively shortens the heat-transfer pathway, minimizes heat losses, and mitigates the formation of local hot spots. The simulated heating energy consumption can be as low as ≈3.94% of the total battery energy. This TMCC design with good tunability opens new frontiers toward smart energy-storage devices in the future from the current collector perspective.

## 1. Introduction

All-solid-state batteries (ASSBs) have attracted intensifying interest as one of the most promising energy-storage devices for portable electronics and electric vehicles due to their great promise of high energy density.[1–3] However, their attainable energy/power density of ASSBs are dramatically reduced because of the sluggish kinetics of lithium-ion transport, especially at room temperature (RT).[4] Normally, the operation of ASSBs requires elevated temperatures.[5–7] Although some ASSBs could be operated at RT, battery energy continues to be low since the employ of low areal electrode loadings and thick solid-state electrolytes (SSEs),[8] and the instable interface issue.[9,10] Among the various SSEs, solid polymer electrolytes (SPEs) possess many prominent advantages, such as excellent flexibility, lightweight, low-cost, and good interfacial contact,[8,11,12] but their limited ionic conductivities (≈$10^{-8}$ to $10^{-6}$ S cm$^{-1}$) at RT has long been identified as one of the knottiest problems. Since SPEs are temperature sensitive, their ionic transfer rate can be increased by two orders of magnitude if a relatively mild temperature (70–90 °C) is granted.[13,14] Thus, auxiliary heating systems, such as environmental chambers, ovens, or temperature incubators, are typically a necessity to demonstrate the advanced performance of ASSBs at the laboratory scale. However, these heating systems are difficult to integrate into practical applications, such as electric vehicles, without compromising battery energy density. In addition to their bulkiness, these systems simultaneously suffer from slow, inhomogeneous heating and severe heat loss. The implementation of a compact, rapid, and uniform thermal modulator is desperately needed, but thus far neglected in ASSB research.

In recent years, battery preheating has been successfully explored for some purposes in lithium-ion batteries, such as enabling fast charging capability,[15–17] or broadening battery operating temperature window.[18–20] In particular, internal preheating can offer higher thermal efficiency due to a much lower heat loss compared to their external preheating counterparts.[21,22] However, in-cell preheating requires high uniformity to avoid local overheating, which could otherwise lead to dendrite formation, side-reactions, or local overcharging.[23] Current collectors (CCs) are crucial parts isolated from the chemical/electrochemical reactions, which are "lithium-ion

Y. Ye, W. Huang, R. Xu, X. Xiao, W. Zhang, H. Chen, J. Wan, F. Liu, H. K. Lee, J. Xu, Z. Zhang, Y. Peng, H. Wang, X. Gao, G. Zhou, Y. Cui
Department of Materials Science and Engineering
Stanford University
Stanford, CA 94305, USA
E-mail: yicui@stanford.edu
Y. Wu
Department of Electrical Engineering
Stanford University
Stanford, CA 94305, USA
Y. Cui
Stanford Institute for Materials and Energy Sciences
SLAC National Accelerator Laboratory
Menlo Park, CA 94025, USA

The ORCID identification number(s) for the author(s) of this article can be found under https://doi.org/10.1002/adma.202202848.

**ADVANCED**
**SCIENCE NEWS**
www.advancedsciencenews.com
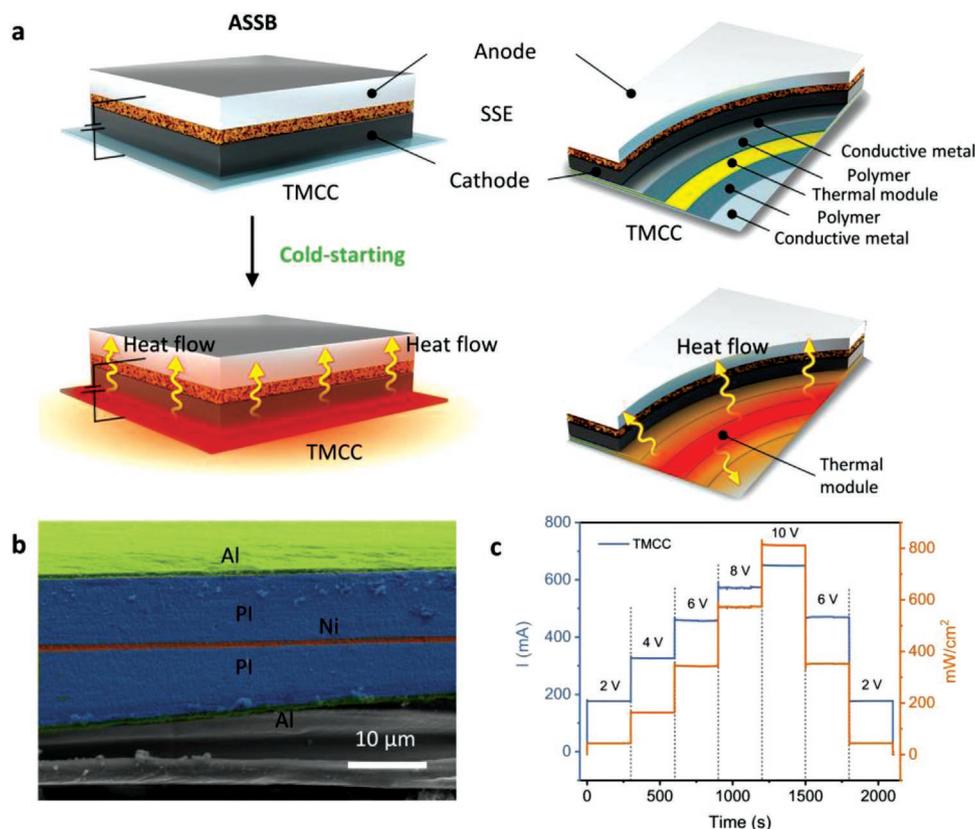
**ADVANCED**
**MATERIALS**
www.advmat.de

**Figure 1.** Concept of an ASSB with TMCC. a) Schematic illustration of an ASSB containing a TMCC. By applying the voltage excitation, Joule heat generates in the middle layer of current collector and spread over the ASSB next to it. b) Cross-sectional SEM image of the TMCC. c) Heating current profile (left axis) and corresponding heating power (right axis) of the TMCC under various voltages.

free" in batteries. Therefore, they could be acting as ideal components for preheating without interfering with regular battery operation. However, CC is generally made of dense and ultralow resistivity materials[24,25] such as copper ($1.68 \times 10^{-8}$ Ω m) or aluminum ($2.65 \times 10^{-8}$ Ω m) and themselves are not suitable to be used as thermal modulator elements directly. The optimal heating will be difficult to achieve if the thermal modulator is tied to the battery cycling circuit due to the following reasons: 1) insufficient heat generation due to the limitation of cycling current, 2) the critical temperature cannot be reached in a short time, and 3) the temperatures cannot be tailored. A new design that could implement battery preheating elements into CC with efficient, controllable, and fast heating capability is therefore highly demanded. Recent advents in the design of lightweight and conductive metal–polymer CCs[26–29] provide new possibilities to design ASSBs with CC preheating.

Here, we report the first thermally modulated CC (TMCC) that enables sub-minute cold-starting ASSB from RT with homogeneous internal cell heating, drastically accelerating the battery kinetics during charging/discharging (**Figure 1**a). Specifically, an ultrathin (≈200 nm) and uniform nickel (Ni) layer is used as the heating modulator and sandwiched between two ultrathin (6 μm) polyimide (PI) layers to isolate heating current from battery cycling current. Subsequently, conductive layers (500 nm-thick, e.g., aluminum) were coated to impart electron

conduction toward the electrode materials. This ultrathin, large-area thermal modulator in CC is critical to: 1) shorten the heat-transfer pathway, 2) minimize heat loss, and 3) mitigate local thermal hotspot formation while being isolated from the chemical/electrochemical reactions inside batteries. As a result, the maximum transient power density of a high areal capacity (≈2.1 mAh cm$^{-2}$) ASSB with TMCC heating is 15-fold compared to one without heating. Moreover, the simulated heating energy consumption is as low as 3.94% of total battery energy, benefiting the thermal efficiency. Our multifunctional CC eliminates the use of auxiliary heating devices that rely on bulk heating and is compatible with current battery manufacturing procedures. This novel architecture design promises great general tunability, which could enable smart energy-storage devices with new functionalities in the future from CC perspective.

## 2. TMCC Configuration and its Stability Characterization

Traditional CCs are made of heavy and dense metal foil, such as Cu for anode CC and Al for cathode CC, which accounts for the high ratio of "dead weight" (>15%) in batteries.[30] To minimize thickness and specific mass, we integrated a thin film heating

layer in the CC center based on our recently designed light-weight CC with PI supporting substrate.[26] The PI substrate isolates the heating modulator from conducting metal layers, which allows for independent electrical pathways for heating and battery cycling. To verify our CC heating hypothesis, a ≈200 nm thick Ni metal is sandwiched with two 6 μm PI films, which subsequently is coated with two ≈500 nm thick Al on two sides as conductive layers to impart electron conductivity to the electrode. As shown in Figure 1b, the total thickness of the composite CC is 13.2 μm, which is close to the commonly used Al CC (≈12 μm). The specific mass of this composite CC is ≈1.41 mg cm$^{-2}$ only 2/5 that of the commonly used Al CC. Thus, the high volumetric energy density of ASSB with TMCC is well maintained (99.63%) and the mass-energy density is improved by 6.01% compared to that with the traditional CC. The ultrathin PI insulating layer with excellent thermal and chemical stability is especially attractive as it provides an exceptional barrier to the polymer electrolyte while allowing rapid heat conduction in the cell.

When the TMCC was assembled in ASSB, uniform Joule heat is generated from the heating modulator by applying current. Since the Ni heating modulation is uniformly adjacent to the conducting layers of CC, each layer of the heating modulator covers the battery unit next to it. Such structure efficiently shortens the heat-transfer time in the cell, alleviates the temperature gradient, and mitigates heat loss. Figure 1c shows the current profile of a TMCC tested at RT. Without further specification, all the cells were assembled with a CC shape of 8 cm × 1 cm. The heating current and power densities increased nonlinearly when the input voltage increased from 2 to 10 V, due to the dependence of ohmic resistance on temperature. The enlarged I–V curve (Figure S1, Supporting Information) illustrates a stable current that can be achieved in ≈2 s as the heating voltage jumps from 6 to 8 V, which demonstrates the fast response and adaptability of this TMCC heating modulator. Further reducing the heating voltage decreases the heating power. The long-term stability of the TMCC was evaluated by both continuous heating and intermittent heating (Figure S2, Supporting Information). The stable current indicates good long-term stability and demonstrates excellent switching capability, both of which hold great promise in practical applications. We used an infrared camera to visualize and validate the heating effect while applying different voltages to the TMCC (Figure S3, Supporting Information). This composite CC can be sealed into pouch cells with no detectable change and withstand extreme conditions with temperatures up to 150 °C.

## 3. ASSBs Assembly with TMCC

Recent reports and analyses show that the adoption of porous polymer hosts with high modulus can successfully increase the energy density of ASSB and suppress the penetration of lithium dendrite.[31–34] PEO–lithium bis(trifluoromethanesulfonyl)imide (PEO–LITFSI) polymer electrolyte is thus utilized as a proof-of-concept for our design. A 12 μm-thick nanoporous polyethylene separator is used as a matrix for PEO–LiTFSI to obtain an ultrathin and highly flexible composite SSE (PEO–LiTFSI–PE). From the cross-sectional scanning electron microscopy (SEM)

image (**Figure 2**a), we find the thickness of PEO–LiTFSI–PE SSE is only 18 μm. Additionally, the pores of the host are fully filled by PEO–LiTFSI and the surface of composite SSE is well covered with PEO–LiTFSI (Figure S4, Supporting Information), ensuring good interfacial contact between SSE and electrode.

We first studied how the TMCC affects the lithium ionic conductivity of composite SSE. An asymmetrical pouch cell was constructed with the composite SSE sandwiched between an Al layer and a TMCC. The heat generated from the Ni layer in the TMCC transfers to composite SSE, increasing its ionic conductivity. The ionic conductivity of the composite SSE increases by two orders of magnitude when heating voltage was increased from 3 to 13 V (Figure 2b). To study the heating and electrochemical behaviors of ASSB equipped with the TMCC, we coated lithium iron phosphate (LFP) onto its surface conductive metal layer as cathode and subsequently paired it with PEO–LiTFSI–PE SSE and a lithium anode. We chose two mild heating conditions (8 and 10 V) for further demonstration. Under both heating conditions, the ionic conductivity can reach $10^{-4}$ S cm$^{-1}$, which meets the basic operational requirement for ASSBs. This in-cell TMCC heating design not only minimizes the heat dissipation to the environment but also provides a compact design without changing the conventional battery configuration. Figure 2c and Figure S5, Supporting Information show the spatial temperature distribution images of the LFP|SSE|Li ASSB under different heating conditions captured by IR camera. Since the heating area is the same as the CC, this TMCC can homogeneously increase the temperature of ASSBs. Compared with the external heating method (such as environmental heating and oven heating), this approach significantly minimizes the temperature gradient and reduces heat loss.

## 4. Heating Speed and Stability of the TMCC in ASSBs

To in situ quantify the heating capability of our thermally modulated CC, a resistance temperature detector (RTD) was placed on the surface of a pouch cell to monitor the temperature change while applying different heating voltages, as schematically shown in Figure 2d. Figure 2e shows the temperature profiles of the ASSB surface under interval heating. The ASSB was first kept at RT for 10 min and then heated under two different heating voltages. Once the heater in TMCC is started, the temperature of the cell quickly reaches an equilibrium between Joule heating and thermal radiation. The stable surface temperatures of the pouch cell are about ≈80–85 °C and ≈105–110 °C for the heating voltages of 8 and 10 V, respectively. Intermittent heating between 0 and 8/10 V shows the fast-switching capability of the TMCC heating modulator. As shown by enlarged temperature-time curves (dotted curves in Figure 2f), the temperatures of the pouch cell can be increased and become steady within ≈40 s under both conditions. We also perform numerical modeling to simulate the heating behavior of the pouch cell with TMCC. The temperature evolution of pouch cell from simulation (solid curves in Figure 2f) is in good consistency with our experimental results, which again confirms the fast-heating capability of our CC heating from RT by a cold-starting mode.
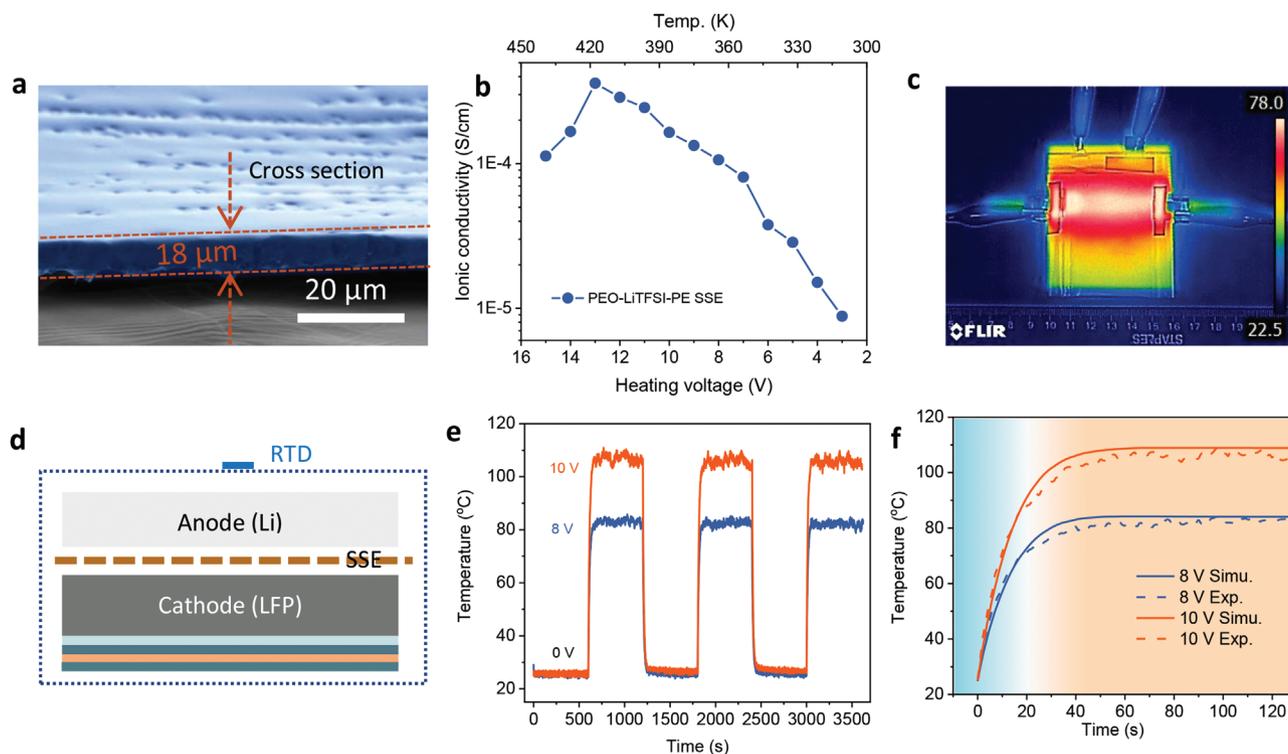
**ADVANCED**
**SCIENCE NEWS**
www.advancedsciencenews.com

**ADVANCED**
**MATERIALS**
www.advmat.de

**Figure 2.** Cold-starting behavior of an ASSB with TMCC. a) SEM image of ultrathin PEO–LiTFSI–PE SSE. b) Arrhenius ionic conductivity ($\sigma$) plots of the PEO–LiTFSI–PE SSE under applying a different voltage through a TMCC. c) IR camera image shows the spatial temperature distribution of the ASSB under passing an 8 V heating voltage through a fixed shape (8 cm × 1 cm) of the TMCC. d) Schematic illustration of the ASSB assembled with RTD to study the temperature change during the cold-starting process. e) Surface temperature behavior of the ASSB under intermittent heating from 0 to 8 V, and from 0 to 10 V, respectively. Each step is held for 10 min. f) Surface temperature vibration of the ASSB during the cold-starting process. Time 0 s represents when heating begins.

## 5. Electrochemical Evaluation of Cold-Started ASSBs with TMCC

High power density is another desired feature for ASSB application but is often neglected in ASSB testing. Here we tested the transient power density of the ASSB and its temperature dependence. **Figure 3**a shows the polarization curves of an LFP|SSE|Li battery using our TMCC by continuously increase the discharge C-rate under different heating conditions. The cells were first fully charged to 4.0 V under 0.1 C at 80 °C and cooled down to RT for further use. Subsequently, the ASSB discharged under different current densities (from 0.5 C to as high as 16.5 C) under a C-rate increasing step of 0.5 C until the discharge voltage is lower than 0.5 V. Each step is maintained for 5 s. The ASSB exhibits reduced polarization curves and higher power densities as the heating voltages increase, implying that the TMCC substantially accelerates the mass transport in the batteries. For the ASSB without TMCC heating, the voltage quickly decreases with discharge C-rate increase, indicating a power output delay due to the limited kinetics of polymeric SSE. In contrast, the ASSB with CC heating shows less decay even under a high output current density, indicating the TMCC heating improves the power performance by increasing the reaction rate and transport kinetics.

Figure 3b shows the corresponding transient power density change of the ASSB under different heating voltages and different discharge current densities. When the discharge current density is increased from 0 to up to 32 mA cm$^{-2}$ the output power densities of ASSB first increase and then decrease, where peak transient output power densities are achieved under specific heating voltages, as shown in Figure 3c. As the heating voltage increases, the transient peak output power density increases, which can be attributed to faster kinetics. Specifically, when the heating voltage increases to 10 V, the peak output power density is as high as ≈50 mW cm$^{-2}$ which is 15× compared to that without heating. To further confirm the enhanced output power density of the ASSB with TMCC, an ASSB pouch cell with a capacity of ≈64 mAh was built to power a ≈290 mW white flashlight (Figure S6, Supporting Information). The cell was first fully charged to 4.0 V at an 80 °C environmental chamber and cooled down to RT before use. The flashlight cannot be lighted up at RT without TMCC heating due to the low power output from the cell. After initiating the heating with a voltage of 8 V, the flashlight can be lighted up under a minute (≈42 s), which further demonstrates the sub-minute cold-starting of ASSB by our novel TMCC heating design.

Based on this heating mechanism, we evaluated the electrochemical performance of the LFP|SSE|Li ASSB by TMCC heating. Without the TMCC heating modulator, the discharge capacity of ASSB (based on LFP mass, loading 9 mg cm$^{-2}$) is less than 30 mAh g$^{-1}$ due to the sluggish kinetics (Figure 3d). Once an 8 V heating voltage is applied to the TMCC, the temperature of the battery increases, which leads to an enhanced
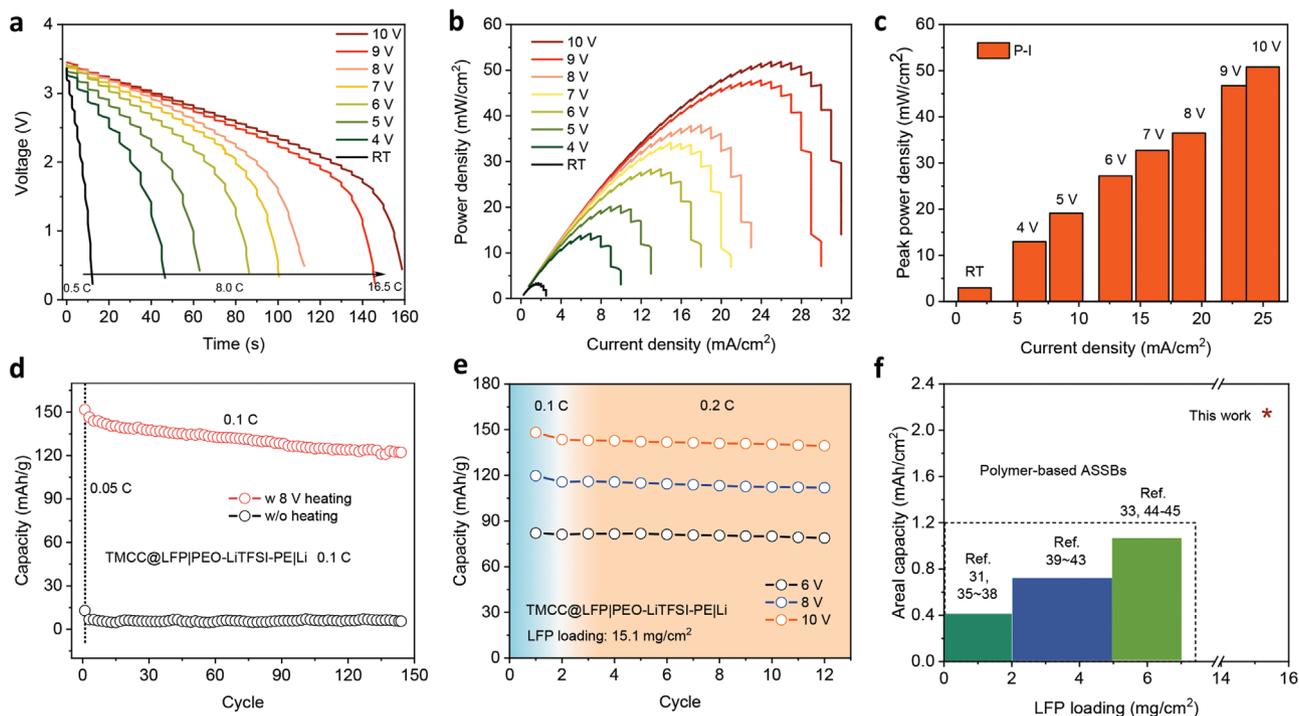
**Figure 3.** Electrochemical performance of an ASSB with TMCC. a) Polarization curves, b) transient power density, and c) peak power density of the ASSB under different TMCC heating conditions. d) Discharge capacities of the LFP|SSE|Li ASSB without TMCC heating and with 8 V TMCC heating operated at room temperature. e) Discharge capacity variation of LFP|SSE|Li cell under different heating voltages at 0.2 C at a high LFP loading of 15.1 mg cm$^{-2}$. Two cycles activation (0.1 C) was applied before long-time 0.2 C cycling. f) Comparison of the LFP loading and areal capacity of the ASSB with recent publications. Most of the batteries in recent publications were tested at auxiliary heating devices.

capacity of ≈140 mAh g$^{-1}$. From the charge–discharge curves (Figure S7, Supporting Information), both the charge and discharge plateaus (3.4 V), and discharge capacity of ASSB with CC heating are like those with liquid electrolytes, demonstrating the excellent electrochemical performance at elevated temperatures enabled by the TMCC. Figure S8, Supporting Information shows the rate performance of the LFP|SSE|Li ASSB under various current rates (from 0.1 C to 6 C, 1 C = 160 mA g$^{-1}$) between 2.5 and 4 V while applying 8 V heating voltage. The ASSB exhibits good rate performance with a capacity around 125 and 100 mAh g$^{-1}$ at 0.4 C and 1 C, respectively. This impressive electrochemical performance mainly arises from the accelerated kinetics by using TMCC. Of note, the ASSB without TMCC heating shows almost negligible capacities and a much lower discharge plateau at RT due to the large polarization (Figure 3d).

To further explore the potential practical vision of our TMCC, we further increased the LFP active materials loading to ≈15 mg cm$^{-2}$ and evaluated its electrochemical performance (Figure 3e). Even with such a high loading, the discharge capacity increased and reached ≈140 mAh g$^{-1}$ at a heating voltage of 10 V, corresponding to an areal capacity of 2.1 mAh cm$^{-2}$. Compared with the recently reported ASSBs using PEO-based SSE (Figure 3f; Table S1, Supporting Information),[31,33,35–45] the ASSB with our TMCC delivers a much higher areal capacity (at least 2×), which holds great promise in increasing the specific energy. Additionally, the polymer-based CC shows good flexibility in the abuse test. As shown in Figure S9, Supporting Information, the LFP|SSE|Li ASSB maintains good functionality powering a red

LED even after folding and unfolding. During the entire folding and unfolding process, the heating current through TMCC remains stable, as shown in Video S1, Supporting Information.

## 6. Heating Energy Consumption

We further utilize numerical simulation to study the heating behavior and associated heating energy consumption of the ASSB at a larger hypothetical size. Such fundamental insight is crucial for the identification of the key parameters for the realization of practical ASSBs with tailorable size and energy density. The CC heater was embedded into every CC layer with the same heating power density to enhance the electrochemical performance of cells or packages (**Figure 4**a). To mimic the heat generation and heat dissipation in real cases, we built three different battery sizes,13.6 Wh, 5 kWh, and 60 kWh, to study their heating consumption (Figure 4b). An additional polyurethane layer (5 mm thick) was used as insulation protection to reduce heating dissipation and save heating energy in each model. To ensure fast kinetic of the ASSB, we chose a working temperature range between 70 and 90 °C in the simulation. Based on this working mechanism, we optimized the heating protocol and then calculated the energy consumption for heating. More simulated parameters can be found in the Experimental Section and Table S2, Supporting Information.

Figure 4c shows the spatial temperature distribution along the thickness of a 4 Ah battery at the end of heating to 90 °C
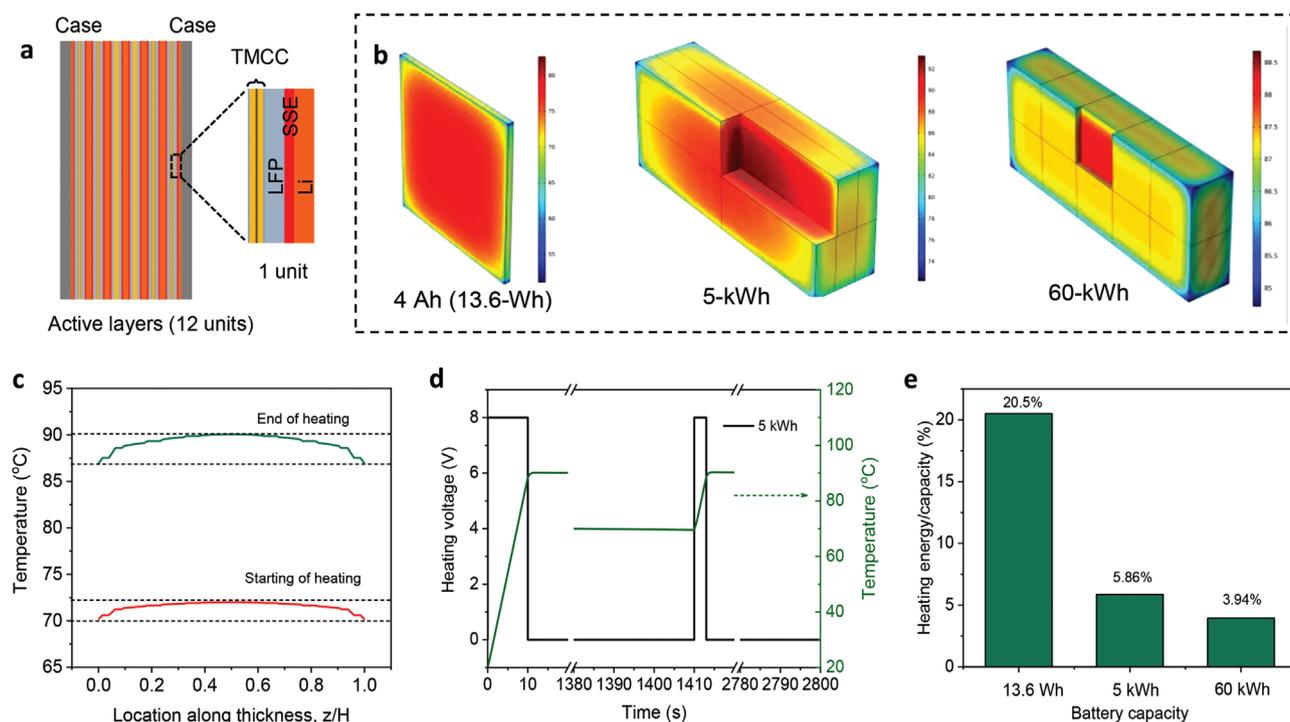
ADVANCED
SCIENCE NEWS
www.advancedsciencenews.com

ADVANCED
MATERIALS
www.advmat.de

**Figure 4.** Heating energy consumption of ASSB based on our TMCC. a) Schematic illustration shows a 13.6 Wh LFP|SSE|Li ASSB configuration for COMSOL simulation. b) Schematic illustrations showing ASSBs with different capacities of 13.6 Wh, 5 kWh, and 60 kWh battery packages. More detailed parameters can be found in Experimental Section and Table S2, Supporting Information. c) Temperature distribution along with the thickness of a 13.6 Wh ASSB. The green line represents the end of heating, and the red line represents the starting of heating. d) The intermittent heating protocol to maintain a 5 kWh battery package operating temperature between 70 and 90° C and its related temperature change. e) Heating energy consumption of different battery sizes based on the optimized heating behavior.

(green curve) and the starting of reheating from 70 °C (red curve). Due to the uniform heating throughout the CC, the corresponding temperature fluctuations are less than 6 °C from battery surface to battery core. Moreover, the temperature gradient from 0.1 z-axis/total height ($z/H$) to 0.9 $z/H$ is very small, demonstrating low heat loss and efficient heating utilization of such CC heating. To optimize the heating protocol, we used a 5 kWh battery package as an example, the TMCC can generate a large amount of Joule heat, which homogenously increases the temperature of the battery pack from RT to 90 °C in 10.5 s. At this time, the voltage applied on the TMCC was turned off, by which the battery temperature slowly decreases to 70 °C in 1400 s. Another heating pulse (3 s) was then applied to re-heat the battery pack to 90 °C again (Figure 4d). Figure 4e compares the ratio of energy consumption during heating to that of the battery capacity under different battery sizes. As the battery size increases, the heating energy consumption decreases due to a reduced surface/volume ratio. In terms of a 1 h operation, the energy dedicated to heating a 60 kWh battery pack is only 3.94% of the total battery energy. It is also noteworthy that our simulation neglects the heat contribution from the exothermic reactions during battery operation, which can further reduce the energy consumption for heating. Based on the achievement made so far, we envision that optimization in practical application is necessary in the future to work in sync with battery management systems, including safety,[46] CC stability,[47] and sensing.

## 7. Conclusion

We have successfully developed a thermally modulated polymer-based CC, which enables sub-minute ASSB cold-starting from RT and substantially enhances battery kinetics. This is enabled by embedding an ultrathin (≈200 nm) heating modulator into the CC, which can generate a significant amount of Joule heat to homogeneously increase the temperature of ASSBs and isolate the heating current from the battery cycling current. The TMCC shows rapid and uniform heating capability, as well as enhanced electrochemical performance. By embedding the TMCC into ASSB, the transient peak output power density of high areal loading of (2.1 mAh cm$^{-2}$) ASSB is 15 times that of one without heating. Numerical simulation demonstrates that this novel TMCC heating strategy is energy efficient and only accounts for 3.94% of the total battery energy. This thermally modulated CC provides a reliable, fast, repeatable, and energy-efficient heating method to enable the use of ASSB from low temperature or RT. This strategy holds great promise for the development of high-specific energy and high-power density ASSB, as well as other smart energy-storage devices.

## 8. Experimental Section

*Thermally Modulated Current Collector Preparation*: A 6 μm-thick PI sheet was prepared based on pyromellitic dianhydride-4,4′-oxydianiline and was used as the substrate. Indeed, 2.5 mmol 4,4′-oxydianiline

**ADVANCED
SCIENCE NEWS**

www.advancedsciencenews.com

**ADVANCED
MATERIALS**

www.advmat.de

(0.751 g, 3.75 mmol) was first added to dimethylformamide (8.6 g) under vigorous stirring. 2.55 mmol PMDA was then added to the solution. The reaction was kept overnight to ensure complete polymerization. Subsequently, the honey-like slurry was coated on glass and dried overnight at RT. After that, the obtained free-standing film was imidized in a box furnace in the glove box to form PI sheet. The temperature ramping program was set as: 1) ramped up from 25 to 100 °C at 3 °C min⁻¹; 2) kept at 100 °C for 30 min; 3) ramped up to 200 °C at 3 °C min⁻¹; 4) kept at 200 °C for 30 min; 5) ramped up to 300 °C at 3 °C min⁻¹; 6) kept at 300 °C for 30 min; 7) cooled down to RT in the furnace. The obtained PI sheet was first rinsed with ethanol, then pretreated with $O_2$ plasma for 5 min to enhance the surficial adhesion. A 200 nm Ni film was deposited on the PI sheet by pulsed DC magnetron sputtering with a pressure less than 10⁻⁶ Torr and argon as protective gas. Another 6 µm-thick PI sheet was then coated on the Ni surface using the abovementioned method while two terminals of the Ni layer were maintained as two tabs. The two sides of the obtained sandwiched film were treated with $O_2$ plasma for 5 min to increase the adhesion force. Subsequently, two 500 nm Al layers were subsequently coated on two sides of the above-sandwiched film as the conducting layers of TMCC.

*Solid-State Electrolyte Preparation*: 0.9 g PEO (Mw = 300 000) and 0.6 g LiTFSI (mass ratio 3:2) were dissolved in 13.5 g acetonitrile (ACN) and mixed by Thicky for 30 min to form a homogenous solution (PEO/LiTFSI). The well-mixed slurry was coated on a 12 µm Cu foil with doctor blade casting (750 µm wet thickness) and then dried in a high-vacuum oven at 60 °C for 4 h. A 12 µm polyethylene separator (Celgard M824) was then placed on the surface and its top surface was wetted by pure ACN solvent. An additional PEO/LiTFSI slurry with a wet thickness of 750 µm was coated on the PE surface. The obtained sample was then dried in the high-vacuum oven at 60 °C for 48 h before further utilization. In this way, PEO/LiTFSI SSE was successfully filled into the PE separator matrix.

*Ionic Conductivity Testing*: The Al/SSE/TMCC asymmetric cell was assembled to measure ionic conductivities of SSE by the electrochemical impedance spectroscopy with the frequency between 0.1 and 10⁶ Hz under different heating voltages.

*ASSB with TMCC Preparation*: LFP cathode (60% LFP, 13% super P carbon black, 2% carbon nanotubes, 15% PEO, and 10% LiTFSI) was dispersed in ACN and coated on above TMCC. The electrodes were completely dried in the vacuum oven at 60 °C before use. The ASSB was assembled with the above cathode, a thin Li foil (50 µm, Hydro-Québec) laminated on 9 µm-thick copper foil as anode and PEO–LiTFSI–PE as a solid-state electrolyte.

*ASSB Heating Behavior by TMCC*: The heating behavior of ASSB (sealed in a pouch case size of 6 cm × 7 cm) assembling with TMCC heater under a specific shape of 8 cm × 1 cm was first evaluated by applying different voltages (0–15 V, Keithley 2200-60-2). The real-time current was recorded to study the heating behavior. IR camera (FLIR, E6) was used to capture the temperature distribution images at different heating conditions. A CC with a heating modulator was then tested using the above methods to record the current change and temperature distribution. For the 64 mAh ASSB, LFP was coated onto two sides of TMCC, and then assembled with eight layers by a laminated method.

*Electrochemical Performance Testing*: All the cells were first resting at 80 °C oven for 3 h to enhance the interfacial contact and then cool down to RT before testing. Keithley 2200-60-2 was used to apply heating voltage on the TMCC. Galvanostatic charge–discharge protocols were conducted on a Land-8 channel battery tester or Biologic VMP3 system. For cold-starting testing, the battery testing and heating were started simultaneously. The LFP|SSE|Li battery was cycled between 2.5 and 4.0 V, and their C rate and specific capacity were calculated based on the mass loadings of the LFP cathode. For rate testing, the Al coating on TMCC was increased to 1.5 µm to ensure high electronic conductivity.

*ASSB Heating Speed Testing*: The RTD (TT-3/100, HBM company) was stuck on the pouch cell surface to in situ record the temperature changing during TMCC operation. A 100 µA current was passed through RTD to record the voltage changing at different temperature.

*COMSOL Simulation*: The temperature evolution of ASSB induced by the Joule heating of TMCC was simulated by COMSOL Multiphysics 5.5. The transient analysis was conducted using the heat-transfer and AC/DC modules integrated in COMSOL. The heating behavior of single unit ASSB was first investigated. The single-layer cell was composed of a CC (Al-PI-Ni), a LFP cathode, a PEO–LiTFSI–PE hybrid SSE, and a Li anode, all of which were assembled in a pouch cell case. Temperature evolution of the cell was co-determined by the Joule heating from the Ni layer in CC as well as the heat loss to the surrounding environment from the cell surface. The Joule heating was induced by applying a constant voltage $V_{app}$ (8 or 10 V) on the Ni layer in a short time. The magnitude of heat loss to the surrounding environment was given by the convective heat flux, $q = h(T_{ext} - T)$, where $q$ is the heat flux, $h$ the heat-transfer coefficient (35 W m⁻² K⁻¹), $T_{ext}$ the external temperature (293 K), and $T$ the temperature of the cell surface. The temperature evolution at the cell surface was collected and compared with experimental results.

Three configurations, multiple-units pouch cell (13.6 Wh), cell group (5 kWh), and cell package (60 kWh), were used to investigate the heating energy consumption with different battery sizes. The multiple-layer cell contained 12 units of single-unit cells, the cell group contained 410 units of multiple-layer cells with an arrangement of 41 × 5 × 2, and the cell package contained 12 units of cell groups with an arrangement of 3 × 2 × 2. For simplicity, the cell group was homogenized as a block with effective thermal properties and a volumetric heat source. The effective thermal properties such as heat capacity and thermal conductivity were obtained from the multiple-layer cell by a homogenization method. The value of the volumetric heat source was calculated by dividing the total Joule heat generated from the Ni layer by the cell volume. In the simulation, the voltage applied on the Ni layer in CC is controlled as "on" and "off" to ensure that the average temperature of ASSB was within the range of 70–90 °C. All the physical properties of the materials are listed in Table S2, Supporting Information.

*Characterizations*: SEM images were taken with a Thermo Fisher Scientific Apreo S LoVac. The impedance spectroscopy measurements to calculate Li ionic conductivity were carried out on a Biologic VMP3 system. Sputter was conducted with a Lesk sputter from the Stanford Nanofabrication Facility (SNF). IR camera (FLIR, E6) was used to capture the temperature distribution of the pouch cell. Microstructural analysis was performed using SEM (Thermo Fisher Scientific Apreo) from the Stanford Nano Shared Facilities (SNSF).

## Supporting Information

Supporting Information is available from the Wiley Online Library or from the author.

## Acknowledgements

## Conflict of Interest

The authors declare no conflict of interest.

## Data Availability Statement

The data that support the findings of this study are available from the corresponding author upon reasonable request.

**ADVANCED
SCIENCE NEWS**

www.advancedsciencenews.com

**ADVANCED
MATERIALS**

www.advmat.de

## Keywords

 [1] Y. Gao, Z. Yan, J. L. Gray, X. He, D. Wang, T. Chen, Q. Huang, Y. C. Li, H. Wang, S. H. Kim, *Nat. Mater.* **2019**, *18*, 384.

 [2] D. H. Tan, A. Banerjee, Z. Chen, Y. S. Meng, *Nat. Nanotechnol.* **2020**, *15*, 170.

 [3] Q. Zhao, S. Stalin, C.-Z. Zhao, L. A. Archer, *Nat. Rev. Mater.* **2020**, *5*, 229.

 [4] S. Deng, M. Jiang, A. Rao, X. Lin, K. Doyle-Davis, J. Liang, C. Yu, R. Li, S. Zhao, L. Zhang, H. Huang, J. Wang, C. V. Singh, X. Sun, *Adv. Funct. Mater.* **2022**, *32*, 2200767.

 [5] Y.-G. Lee, S. Fujiki, C. Jung, N. Suzuki, N. Yashiro, R. Omoda, D.-S. Ko, T. Shiratsuchi, T. Sugimoto, S. Ryu, *Nat. Energy* **2020**, *5*, 299.

 [6] H. Wakayama, H. Yonekura, Y. Kawai, *Chem. Mater.* **2016**, *28*, 4453.

 [7] P. Albertus, V. Anandan, C. Ban, N. Balsara, I. Belharouak, J. Buettner-Garrett, Z. Chen, C. Daniel, M. Doeff, N. J. Dudney, B. Dunn, S. J. Harris, S. Herle, E. Herbert, S. Kalnaus, J. A. Libera, D. Lu, S. Martin, B. D. McCloskey, M. T. McDowell, Y. S. Meng, J. Nanda, J. Sakamoto, E. C. Self, S. Tepavcevic, E. Wachsman, C. Wang, A. S. Westover, J. Xiao, T. Yersak, *ACS Energy Lett.* **2021**, *6*, 1399.

 [8] S. Randau, D. A. Weber, O. Kötz, R. Koerver, P. Braun, A. Weber, E. Ivers-Tiffée, T. Adermann, J. Kulisch, W. G. Zeier, *Nat. Energy* **2020**, *5*, 259.

 [9] Y. Pang, J. Pan, J. Yang, S. Zheng, C. Wang, *Electrochem. Energy Rev.* **2021**, *4*, 169.

[10] R. Xu, F. Liu, Y. Ye, H. Chen, R. R. Yang, Y. Ma, W. Huang, J. Wan, Y. Cui, *Adv. Mater.* **2021**, *33*, 2104009.

[11] K. Xu, *Chem. Rev.* **2014**, *114*, 11503.

[12] W. H. Meyer, *Adv. Mater.* **1998**, *10*, 439.

[13] C. Berthier, W. Gorecki, M. Minier, M. Armand, J. Chabagno, P. Rigaud, *Solid State Ionics* **1983**, *11*, 91.

[14] L. Bandara, M. Dissanayake, B.-E. Mellander, *Electrochim. Acta* **1998**, *43*, 1447.

[15] X.-G. Yang, T. Liu, Y. Gao, S. Ge, Y. Leng, D. Wang, C.-Y. Wang, *Joule* **2019**, *3*, 3002.

[16] X.-G. Yang, G. Zhang, S. Ge, C.-Y. Wang, *Proc. Natl. Acad. Sci. USA* **2018**, *115*, 7266.

[17] H. Ge, J. Huang, J. Zhang, Z. Li, *J. Electrochem. Soc.* **2015**, *163*, A290.

[18] C.-Y. Wang, G. Zhang, S. Ge, T. Xu, Y. Ji, X.-G. Yang, Y. Leng, *Nature* **2016**, *529*, 515.

[19] Y. Ji, C. Y. Wang, *Electrochim. Acta* **2013**, *107*, 664.

[20] X.-G. Yang, T. Liu, C.-Y. Wang, *Nat. Energy* **2021**, *6*, 176.

[21] S. Wu, R. Xiong, H. Li, V. Nian, S. Ma, *J. Energy Storage* **2020**, *27*, 101059.

[22] J. Zhang, H. Ge, Z. Li, Z. Ding, *J. Power Sources* **2015**, *273*, 1030.

[23] H. Wang, Y. Zhu, S. C. Kim, A. Pei, Y. Li, D. T. Boyle, H. Wang, Z. Zhang, Y. Ye, W. Huang, *Proc. Natl. Acad. Sci. U. S. A.* **2020**, *117*, 29453.

[24] Z. Chen, P.-C. Hsu, J. Lopez, Y. Li, J. W. To, N. Liu, C. Wang, S. C. Andrews, J. Liu, Y. Cui, *Nat. Energy* **2016**, *1*, 15009.

[25] M. Yamada, T. Watanabe, T. Gunji, J. Wu, F. Matsumoto, *Electrochem* **2020**, *1*, 124.

[26] Y. Ye, L.-Y. Chou, Y. Liu, H. Wang, H. K. Lee, W. Huang, J. Wan, K. Liu, G. Zhou, Y. Yang, *Nat. Energy* **2020**, *5*, 786.

[27] L. L. Chen, W. L. Song, N. Li, H. Jiao, X. Han, Y. Luo, M. Wang, H. Chen, S. Jiao, D. Fang, *Adv. Mater.* **2020**, *32*, 2001212.

[28] B. Ravdel, F. Puglia, *US9,548,497*, (EaglePicher Technologies, LLC, Joplin, MO, USA) **2017**.

[29] E. Darcy, J. Darst, W. Walker, M. Tran, P. Hughes, S. Nogrady, Z. Awtry, M. Keyser, J. Major, D. Finegan, Metallized Plastic Current Collectors, NASA, Houston, TX, USA **2019**.

[30] L. Hu, J. W. Choi, Y. Yang, S. Jeong, F. L. Mantia, L.-F. Cui, Y. Cui, *Proc. Natl. Acad. Sci. U. S. A.* **2009**, *106*, 21490.

[31] J. Wan, J. Xie, X. Kong, Z. Liu, K. Liu, F. Shi, A. Pei, H. Chen, W. Chen, J. Chen, *Nat. Nanotechnol.* **2019**, *14*, 705.

[32] Y. Cui, J. Wan, Y. Ye, K. Liu, L.-Y. Chou, Y. Cui, *Nano Lett.* **2020**, *20*, 1686.

[33] J. Wu, Z. Rao, Z. Cheng, L. Yuan, Z. Li, Y. Huang, *Adv. Energy Mater.* **2019**, *9*, 1902767.

[34] M. Balaish, J. C. Gonzalez-Rosillo, K. J. Kim, Y. Zhu, Z. D. Hood, J. L. Rupp, *Nat. Energy* **2021**, *1*, 227.

[35] Y. Li, L. Zhang, Z. Sun, G. Gao, S. Lu, M. Zhu, Y. Zhang, Z. Jia, C. Xiao, H. Bu, *J. Mater. Chem. A* **2020**, *8*, 9579.

[36] Z. Lei, J. Shen, W. Zhang, Q. Wang, J. Wang, Y. Deng, C. Wang, *Nano Res.* **2020**, *13*, 2259.

[37] Y. Cheng, J. Shu, L. Xu, Y. Xia, L. Du, G. Zhang, L. Mai, *Adv. Energy Mater.* **2021**, *11*, 2100026.

[38] Z. Wan, D. Lei, W. Yang, C. Liu, K. Shi, X. Hao, L. Shen, W. Lv, B. Li, Q.-H. Yang, F. Kang, Y.-B. He, *Adv. Funct. Mater.* **2019**, *29*, 1805301.

[39] L. Chen, Y. Li, S.-P. Li, L.-Z. Fan, C.-W. Nan, J. B. Goodenough, *Nano Energy* **2018**, *46*, 176.

[40] S. Chen, J. Wang, Z. Zhang, L. Wu, L. Yao, Z. Wei, Y. Deng, D. Xie, X. Yao, X. Xu, *J. Power Sources* **2018**, *387*, 72.

[41] O. Sheng, C. Jin, J. Luo, H. Yuan, H. Huang, Y. Gan, J. Zhang, Y. Xia, C. Liang, W. Zhang, *Nano Lett.* **2018**, *18*, 3104.

[42] X. Ban, W. Zhang, N. Chen, C. Sun, *J. Phys. Chem. C* **2018**, *122*, 9852.

[43] W. Zhou, S. Wang, Y. Li, S. Xin, A. Manthiram, J. B. Goodenough, *J. Am. Chem. Soc.* **2016**, *138*, 9385.

[44] C.-Z. Zhao, X.-Q. Zhang, X.-B. Cheng, R. Zhang, R. Xu, P.-Y. Chen, H.-J. Peng, J.-Q. Huang, Q. Zhang, *Proc. Natl. Acad. Sci. USA* **2017**, *114*, 11069.

[45] T. Thieu, E. Fedeli, O. Garcia-Calvo, I. Combarro, J. Nicolas, I. Urdampilleta, A. Kvasha, *Electrochim. Acta* **2021**, *397*, 139249.

[46] L. Kong, Y. Li, W. Feng, *Electrochem. Energy Rev.* **2021**, *4*, 633.

[47] V. Wurster, C. Engel, H. Graebe, T. Ferber, W. Jaegermann, R. Hausbrand, *J. Electrochem. Soc.* **2019**, *166*, A5410.